

THE HIDDEN MAGNETIC FIELD OF THE YOUNG NEUTRON STAR IN KESTEVEN 79

NATALIA SHABALTAS¹ AND DONG LAI¹
Draft version November 16, 2018

ABSTRACT

Recent observations of the central compact object in the Kesteven 79 supernova remnant show that this neutron star (NS) has a weak dipole magnetic field (a few $\times 10^{10}$ G) but an anomalously large ($\sim 64\%$) pulse fraction in its surface X-ray emission. We explore the idea that a substantial sub-surface magnetic field exists in the NS crust, which produces diffuse hot spots on the stellar surface due to anisotropic heat conduction, and gives rise to the observed X-ray pulsation. We develop a general-purpose method, termed “Temperature Template with Full Transport” (TTFT), that computes the synthetic pulse profile of surface X-ray emission from NSs with arbitrary magnetic field and surface temperature distributions, taking into account magnetic atmosphere opacities, beam pattern, vacuum polarization, and gravitational light bending. We show that a crustal toroidal magnetic field of order a few $\times 10^{14}$ G or higher, varying smoothly across the crust, can produce sufficiently distinct surface hot spots to generate the observed pulse fraction in the Kes 79 NS. This result suggests that substantial sub-surface magnetic fields, much stronger than the “visible” dipole fields, may be buried in the crusts of some young NSs, and such hidden magnetic fields can play an important role in their observational manifestations. The general TTFT tool we have developed can also be used for studying radiation from other magnetic NSs.

Subject headings: stars: neutron – magnetic fields – pulsars: individual (PSR J1852+0040) – X-rays: stars – radiative transfer

1. INTRODUCTION

Magnetic field is perhaps the single most important quantity that determines the observational manifestations of isolated neutron stars (NSs; see, e.g., Turolla 2009; Kaspi 2010). Most of our knowledge of NS magnetic fields is based on the measurement of the rotation period P and period derivative \dot{P} , which, assuming that NS spin-down is due to angular momentum loss through magnetic dipole radiation or magnetic wind, yields estimates for the dipolar magnetic field strength of many NSs. Several NSs are observed to have spectral lines which, when interpreted as electron/ion cyclotron lines or atomic lines, yield a value for the *surface* magnetic field strength (e.g., Ho & Lai 2004; van Kerkwijk & Kaplan 2007; Suleimanov et al. 2010). Neither of these measurements sheds any light on the internal magnetic field configuration. Several recent observations suggest that the internal NS magnetic field must be more complex than a simple dipole. For example, the pulse profiles of X-ray Dim Isolated Neutron Stars may be explained by the addition of higher order multipoles (Zane & Turolla 2006). Also, magnetars are thought to require large toroidal fields to fuel their bursting activity (e.g., Thompson & Duncan 2001). The most striking example of a NS undergoing magnetar-like bursts is SGR 0418+5729, whose observed dipole field ($\lesssim 8 \times 10^{12}$ G) is much too low compared with typical magnetars, and therefore a significant hidden field must be present to power it (Rea et al. 2010; Turolla et al. 2011).

The central compact object (CCO) PSR J1852+0040 in the Kesteven 79 supernova remnant is another source with unusual properties (Halpern & Gotthelf 2010). Specifically, while its dipole surface magnetic field is inferred via P - \dot{P} measurement ($P = 0.105$ s, $\dot{P} = 8.7 \times 10^{-18}$ s s⁻¹) to be only $\sim 3.1 \times 10^{10}$ G, its pulse profile presents with an unusually high pulse fraction ($64 \pm 2\%$), which implies

large temperature anisotropy (concentrated hot spots) on its surface. Such hot spots are unattainable by anisotropic heat conduction at the observed dipole field strength. Also, since the spindown luminosity is much smaller than the X-ray luminosity, they cannot be produced by heating from magnetospheric activities. In this paper we explore a more complex internal field configuration, adding a large crustal toroidal field aligned about the magnetic dipole axis to suppress heat conduction everywhere except toward the magnetic poles of the NS. While the idea of using crustal field to suppress heat conduction is not new (e.g., Geppert et al. 2004, 2006), our goal is to use the observed X-ray light curve to quantitatively constrain the magnitude and shape of this hidden toroidal field.

To quantitatively model the X-ray light curve of a magnetic NS, it is necessary to add up emissions from all surface patches of the star, taking account of beaming/anisotropy due to magnetic fields and light bending due to general relativity (Zane & Turolla 2006). While this is conceptually straightforward, it is not easy to implement in practice, as atmosphere models for many surface patches (each with different T_{eff} and \mathbf{B}) are needed. Therefore, in Section 2 we develop a practical method, termed “Temperature Template with Full Transport” (TTFT), for computing radiation intensity from different surface patches. This method captures the essential features of radiation from magnetic atmospheres, but does not require full self-consistent atmosphere modeling for each surface patch. The TTFT method allows us to compute NS light curves with arbitrary surface magnetic field and temperature distributions. In Section 3, we study various crustal magnetic field configurations, present the resulting surface effective temperature distributions, and apply the method of Section 2 to compute the pulse profiles and reproduce the observed high pulse fraction of the CCO in Kes 79. We

¹ Center for Space Research, Department of Astronomy, Cornell University, Ithaca, NY 14853, USA

discuss the results in Section 4, and conclude with Section 5.

2. LIGHT CURVE CALCULATION AND THE TTFT METHOD

In this section we outline our method for computing X-ray light curves for NSs with arbitrary surface magnetic field and temperature distributions. Although our application focuses on the CCO in Kes 79 (Section 3), the method presented here is general and can be applied to other types of magnetic NSs with atmospheres.²

2.1. Light Curve Calculation

The observed specific radiation flux dF_ν^o due to an infinitesimal patch (area dA) on the NS surface is given by

$$dF_\nu^o = I_\nu^o d\Omega^o = \frac{g}{D^2} I_\nu^e(\mathbf{k}) \cos \alpha \left| \frac{d \cos \alpha}{d\mu} \right| dA, \quad (1)$$

where I_ν^o is the observed specific intensity; $d\Omega^o$ is the observed angular size; g is the gravitational redshift factor given by $g^2 \equiv (1 - 2GM/Rc^2)$; M , R , and D are the mass, radius, and distance to the NS; I_ν^e is the local specific intensity (as emitted at the surface patch of the NS); \mathbf{k} is the direction of photon propagation at the surface; $\alpha \equiv \cos^{-1}(\mathbf{k} \cdot \hat{\mathbf{r}})$ is the angle between \mathbf{k} and the local radial vector; and μ is the cosine of the polar angle (with respect to the observation axis) of the patch. Due to gravitational light bending, $\cos \alpha$ is a non-trivial function of μ . Following Beloborodov (2002), we make an approximation to this function, and calculate the observed specific flux as

$$F_\nu^o \simeq \int \frac{g^3}{D^2} I_\nu^e(\mathbf{k}) [1 - g^2(1 - \mu)] dA, \quad (2)$$

where the integration is over the entire observable area (including light bending) of the NS surface. Thus, given the knowledge of local radiative intensity [$I_\nu^e(\mathbf{k})$] of all surface patches, combined with the photon trajectory at different rotational phase (time) [$\mu(t) \Leftrightarrow \alpha(t)$], the resultant observed specific flux can be calculated.

2.2. Radiative Transfer in Magnetic Neutron Star Atmospheres

The full computation of $I_\nu^e(\mathbf{k})$ requires construction of atmospheric models in radiative equilibrium for various surface magnetic fields \mathbf{B} (magnitude and direction), effective temperatures T_{eff} , and compositions (e.g., Shibano et al. 1992; Pavlov et al. 1995; Zane et al. 2001; Ho & Lai 2001, 2003, 2004; Potekhin et al. 2004; van Adelsberg & Lai 2006; Suleimanov et al. 2010). This is currently not practical for exploration of a wide range of model parameters, since quantitative calculation of the light curve demands adding up many different surface patches (rather than one or two hot spots; cf. Ho 2007). Therefore we develop an approximate method (TTFT) (see Section 2.3) that allows us to obtain $I_\nu^e(\mathbf{k})$ efficiently. Here, we describe our full radiative transfer calculation in NS atmospheres.

In the atmospheres of magnetized NSs, photon polarization plays an important role in determining $I_\nu^e(\mathbf{k})$. For example, at photon frequencies smaller than the electron cyclotron frequency, the mean free path for ordinary (O)

mode photons is much smaller than that of the extraordinary (X) mode photons, and therefore, the X-mode photons that contribute to the emergent flux are typically produced in the deeper, hotter layers of the atmosphere. At higher field strengths ($\gtrsim 8 \times 10^{13}$ G), vacuum polarization will also have a strong effect on the radiation spectrum (Lai & Ho 2002, 2003). While rigorous treatment of this effect is available (van Adelsberg & Lai 2006), we describe an approximate method below.

For a photon of a given energy E propagating along \mathbf{k} in the NS atmosphere, vacuum resonance occurs at

$$\rho_V = 0.96 Y_e^{-1} E_1^2 B_{14}^2 f_B^{-2} \text{ g cm}^{-3}, \quad (3)$$

where Y_e is the electron fraction, $E_1 = E/(1 \text{ keV})$, $B_{14} = B/(10^{14} \text{ G})$, and f_B is a slowly varying function of B , of order unity. At resonance, the X and O polarization modes become degenerate, and therefore the photon may be converted from one mode to another when it traverses the resonance. We define two more effective polarizations modes: + and -. These modes act as X (O) polarization modes before the resonance and as O (X) modes after. Lai & Ho (2002) showed that photons satisfying the adiabatic condition, $E \gtrsim E_{\text{ad}}$, act as + and - modes. Here

$$E_{\text{ad}} = 2.52 \left[f_B \tan \theta_{kB} |1 - (E_{Bi}/E)^2| \right]^{2/3} \left(\frac{1 \text{ cm}}{H_\rho} \right)^{1/3} \text{ keV}, \quad (4)$$

where $\theta_{kB} \equiv \cos^{-1} \mathbf{k} \cdot \hat{\mathbf{B}}$, $E_{Bi} = 0.63 Y_e B_{14} \text{ keV}$ is the ion cyclotron energy, and $H_\rho \equiv |ds/d \ln \rho|$ is the density scale height along the ray. More generally, a photon with energy $E \sim E_{\text{ad}}$ will have a nonadiabatic ‘jump’ probability of

$$P_{\text{jump}} = \exp \left[-\frac{\pi}{2} (E/E_{\text{ad}})^3 \right]. \quad (5)$$

If the ‘jump’ probability is low, most outward diffusing photons will evolve through the resonance adiabatically as + or - modes, undergoing mode conversion. On the other hand, if the ‘jump’ probability is high, X-mode (O-mode) photons will remain X-mode (O-mode) photons after traversing the resonance. We therefore elect to treat the X, O, +, and - photon modes as distinct carriers whose relative abundances are determined by P_{jump} :

$$I_\nu^e = P_{\text{jump}}(I_\nu^X + I_\nu^O) + (1 - P_{\text{jump}})(I_\nu^+ + I_\nu^-). \quad (6)$$

Note that, for the application to the Kes 79 CCO (Section 3), at fields $B \sim 10^{10} - 10^{11}$ G and energies $E \sim 1 - 5$ keV, ρ_V is smaller than the photosphere densities, and therefore vacuum polarization does not play an important role. We therefore treat all photons as “jump” photons ($P_{\text{jump}} = 1$), and do not compute intensities for the + and - modes.

In general, to compute the individual specific intensities for each carrier, we integrate the standard radiative transfer equation, $dI_\nu^i/d\tau_\nu^i = B_\nu - I_\nu^i$. However, for the present purposes it is sufficient to use the Eddington-Barbier relation:

$$I_\nu^i(\mathbf{k}) \approx \frac{1}{2} B_\nu [T(\tau_\nu^i(\mathbf{k}) = 2/3)]. \quad (7)$$

² We do not consider the extreme case of high magnetic field at low temperature, for which the NS surface may be in condensed form (e.g., Lai & Salpeter 1997; Medin & Lai 2007).

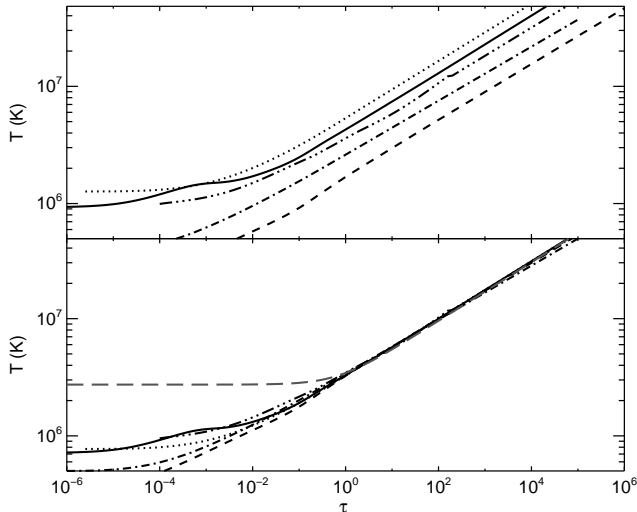


FIG. 1.— *Top panel:* NS atmosphere temperature profiles vs Thomson depth from several self-consistent atmosphere models. Solid line – $B = 6.2 \times 10^{10}$ G, $T_{\text{eff}} = 4 \times 10^6$ K; dashed line – $B = 6.2 \times 10^{10}$ G, $T_{\text{eff}} = 1 \times 10^6$ K; dotted line – $B = 0$, $T_{\text{eff}} = 5 \times 10^6$ K; dashed-dotted line – $B = 0$, $T_{\text{eff}} = 1.6 \times 10^6$ K; dashed-triple-dotted line – $B = 2 \times 10^{12}$ G, $T_{\text{eff}} = 5 \times 10^6$ K. *Bottom panel:* The same profiles rescaled such that $T_{\text{eff}} = 3.8 \times 10^6$ K at a normal magnetic field with strength $B = 8.8 \times 10^{10}$ G using the TTFT method. In addition, we include the Thomson grey opacity temperature profile $T^4 \sim (\tau + 2/3)$ (long dashed), similarly rescaled.

That is, the emergent intensity (toward \mathbf{k}) due to carrier i is equal to the Planck function evaluated at the depth at which the optical depth τ_ν^i for that carrier (along \mathbf{k} , measured from the outside in) is equal to $2/3$. The factor of $1/2$ arises because the photon number distribution is split among two carriers at all times. Thus, to calculate the total emergent specific intensity, only a few pieces of information are required. These are: the direction and magnitude of the magnetic field, the opacities for each carrier, and the atmospheric temperature and density profiles [$T(\tau)$ and $\rho(\tau)$, where $\tau = \kappa_T y$ (with $\kappa_T = 0.4 \text{ cm}^2 \text{ g}^{-1}$) is the (zero-field) Thomson depth, and y is the column density].

We use free-free absorption opacities for each carrier, including the contribution of electron-ion Coulomb collisions, as described by Lai & Ho (2003). This opacity depends strongly on $\mathbf{k} \cdot \hat{\mathbf{B}}$, as well as on density and temperature.

In addition, at the magnetic field strengths we are considering, the opacity is further complicated by oscillations in the magnetic Gaunt factor (Potekhin 2010). However, the energies we consider have values of $\sim 1.5 - 5$ times the electron cyclotron energy and therefore these oscillations are not very strong. Furthermore, while the oscillations may affect the specific flux emitted at certain frequencies, we do not expect them to affect pulse shape. We therefore do not include this complication in our calculation, instead choosing to use the non-magnetic Gaunt factor, which captures the trend about which the full magnetic Gaunt factor oscillates.

The temperature profile $T(\tau)$ and density profile $\rho(\tau)$ are related by the equation of hydrostatic equilibrium. For all practical purposes, an ideal, non-degenerate gas equation of state can be used with better than a few percent accuracy (e.g., Ho & Lai 2001).

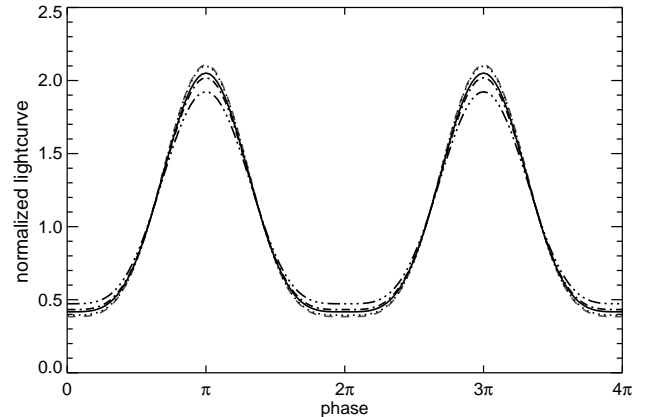


FIG. 2.— Sample full-star light curves of NS surface emission at photon energies around 1.5 keV calculated using the TTFT method. Two rotation phases are shown. These light curves are computed for a specific NS surface temperature and magnetic field distributions and viewing geometry (see Section 3). The different curves correspond to the results obtained using different temperature profile templates as depicted in Figure 1. The highest pulse fraction obtained is 62%, and the lowest 53%.

2.3. TTFT: A Method for Temperature Profile Computation

As an all-purpose tool, the computational procedure described in Sections 2.1-2.2 requires the knowledge of the atmospheric temperature profile $T(\tau)$. In theory, for a given combination of effective temperature, magnetic field strength and direction, $T(\tau)$ is obtained by self-consistent atmosphere modeling to achieve radiative equilibrium. However, this modeling must be done for every single patch of the NS surface, and is not practical to implement. Here we propose the “Temperature Template with Full Transport” (TTFT) method for constructing temperature profiles. While this method is not accurate for predicting the observed synthetic radiation spectrum, we show that it is reliable insofar as light curve shape (and therefore pulse fraction) is concerned.

The TTFT method consists of the following steps: (i) We write the temperature profile in the form $T(\tau) = T_0 F(\tau)$, characterized by the dimensionless template function $F(\tau)$ and the adjustable constant T_0 . The template function may be obtained from a specific NS atmosphere model. (ii) For each $T(\tau)$, we carry out full radiative transfer calculation (Section 2.2) to obtain the total radiation flux from a single surface patch,

$$\mathcal{F} = \int d\nu \int d^2\mathbf{k} I_\nu^e(\mathbf{k}) \mathbf{k} \cdot \hat{\mathbf{r}}, \quad (8)$$

where the integration $\int d^2\mathbf{k}$ covers the outgoing direction relative to the surface normal vector $\hat{\mathbf{r}}$. Since $\mathcal{F} = \sigma T_{\text{eff}}^4$, we then obtain a one-to-one mapping between T_0 and T_{eff} for the given template function $F(\tau)$. (iii) We then adopt the *ansatz* that for a given surface patch with T_{eff} , the atmosphere profile is $T(\tau; T_{\text{eff}}) = T_0(T_{\text{eff}})F(\tau)$, and the emergent radiation intensity can be computed via the method of Section 2.2.

Figure 1 demonstrates the reasoning for the validity of the TTFT method. The top panel presents several self-consistent temperature profiles at different effective temperatures and field strengths provided by Wynn Ho ($B = 0$ and $B = 2 \times 10^{12}$ G models) and by Valery Suleimanov ($B = 6.2 \times 10^{10}$ G models). We note that all the profiles

are very similar in shape, especially for $\tau \gtrsim 0.1$, and differ mostly in overall normalization; this is true both with respect to magnetic field strength variation and effective temperature variation. After normalization to the same $T_{\text{eff}} = 3.8 \times 10^6$ K and $B = 8.8 \times 10^{10}$ G, all the temperature profiles become similar at $\tau \gtrsim 0.1$. Therefore, when computing the intensity of photons that emerge from sufficient depth in the atmosphere, the same single temperature template $F(\tau)$ may be used for the entirety of the NS surface.

Note that it is not surprising that all the temperature profiles are essentially identical at $\tau > 1$; indeed, in the diffusion-limited regime that is to be expected. The less obvious and most crucial point is that the profiles remain very similar for $0.1 < \tau < 1$, where they also differ significantly from a grey opacity profile. In our computations of synthetic light curves (see Figure 2), we see that only the photons traveling nearly radially out from the star emerge from slightly deeper than $\tau \sim 1$, and thus most of the photons contributing to the light curve emerge from smaller Thomson depths. Therefore, a grey opacity temperature profile could not possibly produce the same large synthetic pulse fraction, and would not yield a realistic representation of the emergent flux; we *must* use a self-consistent template accounting for depth-dependent opacity.

Figure 2 shows sample X-ray light curves (normalized to a mean of unity) of magnetic NS surface emission, computed using our TTFT method with various template functions $F(\tau)$ depicted in Figure 1. These light curves are for a specific NS surface model (effective temperature and magnetic field distributions) appropriate for the CCO in Kes 79 (see Section 3 for details). We see that the shapes of these light curves are very similar, with the pulse fraction ranging from 53% to 62%, despite the fact that the template functions are obtained from vastly different atmosphere models. Note that in renormalizing the temperature profile (to obtain the T_0 - T_{eff} mapping), we make the approximation that the magnetic field is normal to the stellar surface, and we keep its magnitude always set to the field strength at the magnetic poles. This speeds up the construction of the temperature profile (i.e., the T_0 - T_{eff} mapping for a given template function) since the integration in Equation (8) can be done more efficiently, and need not be repeated for every surface patch. We have found that this approximation introduces rather small error in the resulting T_0 - T_{eff} relation; this is understandable because T_{eff} is determined by summing over the emitted spectrum in all directions, and the direction of the magnetic field is averaged over, while the radiative transfer is not too sensitive to factor-of-two changes in field strength. Nevertheless, we note that when computing $I_\nu^e(\mathbf{k})$ for the light curve, the “correct” magnetic strength and direction must be adopted in order to accurately account for the magnetic beaming effect.

3. CONSTRAINING THE CRUSTAL MAGNETIC FIELD OF THE NEUTRON STAR IN KES 79

We now use the method described in Section 2 to model the X-ray light curve of the NS in Kes 79, thereby constraining the magnetic field configuration in the NS crust.

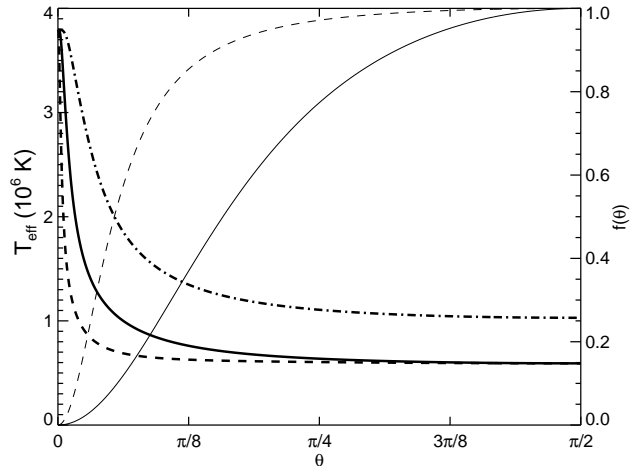


FIG. 3.— Effective surface temperature distribution $T_{\text{eff}}(\theta)$ (heavy lines) for different crustal magnetic field configurations. The toroidal field is characterized by Equations (9)-(10). Solid line – $B_0 = 2 \times 10^{14}$ G, $\theta_0 = 40^\circ$; dashed line – $B_0 = 2 \times 10^{14}$ G, $\theta_0 = 10^\circ$; dot-dashed line – $B_0 = 2 \times 10^{13}$ G, $\theta_0 = 40^\circ$. The light lines show the corresponding function $f(\theta)$ at different θ_0 .

An internal field of strength similar to the inferred dipole field of the Kes 79 NS would lead to a very uniform temperature distribution on the NS surface (e.g., Schaaf 1990; Potekhin et al. 2003). In order to produce sufficiently concentrated hot spots, we introduce a toroidal (with respect to the dipole axis) component to the magnetic field, such that it is sufficiently large everywhere except in a concentrated region around the magnetic axis. We adopt the following form for the toroidal field:

$$B_\phi(r, \theta) = B_0 f(\theta) g(r), \quad (9)$$

where B_0 is an adjustable maximum field strength and θ is the magnetic colatitude.

Because the NS atmosphere is likely too tenuous to be able to sustain a toroidal field, the toroidal field should be contained entirely in the crust, such that the poloidal current producing it is also contained in the crust. Thus, a realistic form of $g(r)$ should vanish at least at the NS surface, and possibly at the crust-core interface as well. However, for simplicity, in the present calculation we treat $g(r)$ as constant. We choose the following functional form for f :

$$f(\theta) = \frac{f_0 (\sin \theta / \sin \theta_0)^2}{1 + (\sin \theta / \sin \theta_0)^2}, \quad (10)$$

where θ_0 is an adjustable parameter defining how sharply the toroidal field rises away from the magnetic poles. The normalization constant f_0 is specified so that $\max[f(\theta)] = 1$. Obviously, this functional form for $f(\theta)$ is representative; other forms are possible. However, the detailed shape of $f(\theta)$ cannot be realistically constrained and is not important for our purpose. Our goal is to examine what ranges of values of B_0 and θ_0 are required in order to produce sufficiently distinct surface hot spots to generate the observed large pulse fraction in Kes 79 NS. Note that we are essentially exploring a parameter space orthogonal to the one considered by Geppert et al. (2006), who fixed $f(\theta)$ to be a simple sinusoid and explored the dependence of surface temperature and pulse shape on $g(r)$.

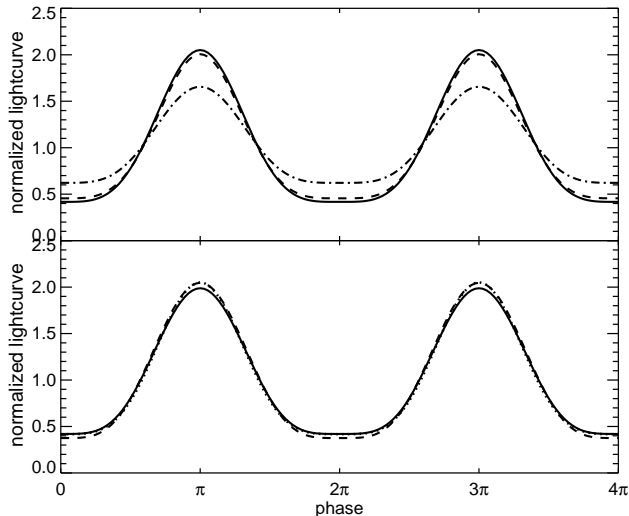


FIG. 4.— *Top panel:* Full-star synthetic light curves at photon energies around 1.5 keV for different crustal magnetic fields. The different lines correspond to the different effective temperature distributions $T_{\text{eff}}(\theta)$ depicted in Figure 3. The pulse fractions are 58% (solid line), 55% (dashed line) and 38% (dot-dashed line). *Bottom panel:* Light curves for the $B_0 = 2 \times 10^{14}$ G, $\theta_0 = 40^\circ$ model at different photon energies: $E \sim 1.5$ keV (dotted line, pulse fraction 58%), $E \sim 3$ keV (solid line, PF 58%) and $E \sim 5$ keV (dashed line, PF 63%).

In addition to the crustal toroidal magnetic field, we also include a star-centered dipole field. The canonical surface dipole field strength (at the magnetic poles) as inferred from the $P-\dot{P}$ measurement is $B_p \sin \theta_B \simeq 6.2 \times 10^{10}$ G (for $R = 10$ km and moment of inertia $\simeq 10^{45}$ g cm²), where θ_B is the angle between the magnetic axis and the spin axis. Of course, pulsar spindown power is not exactly given by the vacuum dipole radiation formula (Contopoulos & Spitkovsky 2006). For concreteness, we adopt $B_p \simeq 8.8 \times 10^{10}$ G in our calculations (corresponding to $\theta_B = 45^\circ$), although using a somewhat different value (within a factor of two) would only have a small effect on our result.

Given the magnetic field configuration, the effective temperature distribution on the NS surface is determined by heat conduction in the crust (e.g., Schaaf 1990; Heyl & Hernquist 1998; Potekhin & Yakovlev 2001). Since the magnetic field is symmetric about the magnetic axis, the effective temperature depends only on the polar angle, $T_{\text{eff}} = T_{\text{eff}}(\theta)$. We use the zero-accretion fitting formula of Potekhin et al. (2003) to calculate $T_{\text{eff}}(\theta)$. This formula takes as inputs a core temperature and a crustal magnetic field of arbitrary strength and direction (assumed constant through the radial extent of the crust), and returns the effective surface temperature. We fix the core temperature at $T_c = 10^9$ K, corresponding to $T_{\text{eff}} = 3.8 \times 10^6$ K at the magnetic poles, which matches sufficiently the hot spot temperature expected from blackbody fits.

Figure 3 presents three sample functions $T_{\text{eff}}(\theta)$, two at the same value of B_0 but different values of θ_0 and one at a lower value of B_0 . We also include the corresponding $f(\theta)$ curves to clarify the effect of changing θ_0 . It is important to note that when the toroidal field strength B_0 is sufficiently large, even a very smooth B_ϕ profile can produce rather small hot spots. For example, at $B_0 = 2 \times 10^{14}$ G and $\theta_0 = 40^\circ$, the temperature drops from $T_p \simeq 4 \times 10^6$ K

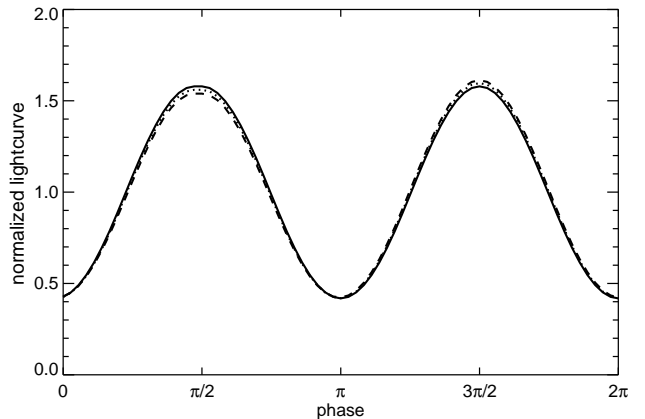


FIG. 5.— Full-NS light curves at $B_0 = 2 \times 10^{14}$ G, $\theta_0 = 40^\circ$, $E = 1.5$ keV, and different geometries. Solid – $\beta = 80^\circ$, $\theta_B = 90^\circ$. Dotted – $\beta = 80^\circ$, $\theta_B = 85^\circ$. Dashed – $\beta = 80^\circ$, $\theta_B = 80^\circ$.

at the magnetic pole to $T_p/2$ at $\theta \sim 3^\circ$, and to $T_p/4$ at $\theta \sim 10^\circ$.

When computing the synthetic X-ray light curves, we split the effective temperature curve into 7-9 bins, with degree-resolution close to the pole, and coarser resolution for the rest of the star. For each bin we create the temperature profile $T(\tau; T_{\text{eff}})$ at the requisite effective temperature using the TTFT process described in Section 2. Note that since B_ϕ vanishes at the NS surface, it does not contribute to the atmospheric physics in any way. We can then compute the light curves for each of the effective temperature distributions depicted in Figure 3.

In addition to B_0 and θ_0 , the light curves also depend on two geometrical parameters: the angle between the line of sight and the rotation axis, β , and the angle between the magnetic dipole axis and the rotation axis, θ_B . We select β and θ_B in order to maximize the pulse fraction. Since, as a rule, emission is strongest for photons emitted parallel to the direction of the magnetic field, we should select β and θ_B to be the same or nearly so, such that at some point during the NS’s rotation, the photons we see are emitted parallel to the magnetic field and the beaming effect is maximized. We also select the angles such that a single-peaked pulse profile is produced (see below for double-peaked profiles). After exploring the available phase space, we settle on $\beta = \theta_B = 45^\circ$. This choice is not an overly specific one, however, as there are many other geometrical configurations that result in only slightly smaller pulse fractions. Our selection of β and θ_B maximizes the pulse fraction, and therefore minimizes how “dark” the stellar surface must be away from the hot spots. This selection is therefore the most conservative estimate of the required strength of B_ϕ .

The top panel of Figure 4 presents the whole-star synthetic light curves at the photon energy $E = 1.5$ keV, using each of the three $T_{\text{eff}}(\theta)$ functions of Figure 3. The $B_0 = 2 \times 10^{14}$ G, $\theta_0 = 40^\circ$ model (solid line) achieves the required pulse fraction observed in Kes 79 NS. For $B_0 = 2 \times 10^{14}$ G, $\theta_0 = 10^\circ$ model (dashed line), the hot spot is too concentrated with a small area, causing a decrease in pulse fraction. For $B_0 = 2 \times 10^{13}$ G, $\theta_0 = 40^\circ$ model (dot-dashed line), the spot has enough area, but the rest of the star is simply not dark enough, and thus the pulse fraction is small. We therefore conclude that a toroidal magnetic field in the crust of order

$B_\phi \sim$ a few $\times 10^{14}$ G or higher, rising slowly enough from zero toward the magnetic equator, such that it allows the hot spot to gain enough area, can naturally produce the requisite pulse fraction observed in the Kes 79 NS.

The bottom panel of Figure 4 shows that the pulse profiles at different photon energies are approximately the same (with the pulse fraction slightly higher at $E = 5$ keV than at 1.5 keV), in agreement with the observation of the Kes 79 NS (Halpern & Gotthelf 2010). Note that while we compute the pulse profiles at a single well-defined energy, they are nevertheless representative of the pulse profiles that would be observed in energy bins centered on the quoted energies, with widths of a few tenths of a keV.

Although our theoretical light curves reproduce the large pulse fraction observed in the Kes 79 NS, there remains appreciable difference between the shape of the light curves presented in Figure 4 and the observation. Our model light curves have relatively sharp peaks, with the system spending nearly half of the rotation period at the (observed) flux minimum. This is different from the broad flux maximum observed in Kes 79 NS. Note, of course, that we have only considered one particular functional form for the magnetic field distribution, and the form we consider is very smooth. It is not clear that more complex magnetic field configurations would yield the right pulse shape while maintaining a high pulse fraction. Another possible way to resolve this difference is to consider pulse profiles with two peaks per rotation period, one peak for each magnetic hot spot. This is possible when both the line of sight and the magnetic dipole axis are nearly perpendicular to the rotation axis. Such a light curve would be observationally indistinguishable from a single-peaked light curve, but would imply that the actual rotation period of the NS is two times shorter.

Figure 5 presents several examples of the two-peaked light curves for different combinations of the geometric parameters β and θ_B (both around 90°). We see that the width of the peaks is much closer to what is observed in Kes 79 NS. Obviously, when either β or θ_B deviates significantly from 90° , the two peaks will have unequal heights, which can be measurable. Still, our result in Figure 5 shows that the square of geometrical phase space with corners at $(\beta, \theta_B) = (80^\circ, 80^\circ)$ and (by symmetry) $(110^\circ, 110^\circ)$ provides viable two-peaked light curves that may be indistinguishable from single-peaked light curves.

4. DISCUSSION

4.1. Large Pulse Fraction - How?

Beloborodov (2002) demonstrated that two infinitesimal antipodal hot spots, emitting isotropically, on the surface of a $1.4M_{\text{sun}}$, 10 km NS cannot, in full geometric generality, produce light curves with pulse fractions higher than about 12%. Poutanen & Beloborodov (2006) later generalized this to anisotropic emergent intensities, producing pulse fractions of a few $\times 10\%$. Thus, it seems that even if one were to find a way to create hot spots on the NS surface, it would be difficult produce the 60% pulse fraction observed in Kes 79 NS. How, then, did we accomplish this?

In fact, diffuse hot spots of finite size (with varying temperatures), combined with the beaming due to anisotropic photon opacities in magnetic fields, are essential for gen-

erating the large pulse fraction in our model. In our calculations, the hottest regions with radii of $\sim 0.5^\circ$ around each magnetic pole do not produce pulse fractions higher than about 40%. Instead, it is the subsequent annuli of decreasing effective temperature that create the bulk of the pulsed emission. Therefore, to quantitatively model the light curves of NS surface emission, it is important to go beyond the single-temperature hot spot approximation widely used in many previous studies. It is for this reason that a reasonably efficient method, such as TTFT developed in Section 2, is necessary in order to add up atmosphere emissions from many different patches of the NS surface to produce synthetic light curves.

4.2. Crustal Magnetic Field Evolutionary Timescale

The crustal magnetic field assumed in our model (Section 3) is unlikely to be unique for producing the observed light curve of Kes 79 NS. In a way, it is the most conservative magnetic configuration, with the minimum number of free parameters, and allows for self-consistent calculation of the surface temperature distribution and the resulting light curve. One can invoke more complex magnetic field topology, but the general conclusion of our result, that the NS in Kes 79 contains a significant hidden magnetic field (of order a few $\times 10^{14}$ G or larger) in the bulk region of its crust, is likely to be robust. We also note that while the “strong toroidal field + weak dipole field” configuration adopted in our model has generally been thought to be unstable in fluid stars (e.g., Braithwaite & Nordlund 2006; Reisenegger 2009), this may not, in fact, be the case, as Braithwaite (2009) demonstrated that the effect of gravitational stratification is such that even a relatively weak poloidal field can be enough to stabilize the configuration. In NSs beyond the fluid stage of evolution, the crust also has a stabilizing effect. If we include a poloidal field of similar strength as the toroidal field, our general conclusion will be unchanged.

While it is beyond the scope of this paper to speculate how the magnetic field configuration adopted in our model may come about, we can estimate how long this magnetic field configuration lasts in its current form to allow for a good chance of being observed. Given the toroidal field strength we have found above for Kes 79 ($\sim 10^{14}$ G), its evolution should be dominated by Hall drift, since the Ohmic timescale for a young NS is much longer than the Hall timescale (see Reisenegger et al. 2005; Pons & Geppert 2007; Pons et al. 2009):

$$\frac{\partial \mathbf{B}}{\partial t} = -\nabla \times \left[\frac{c}{4\pi n_e e} (\nabla \times \mathbf{B}) \times \mathbf{B} \right], \quad (11)$$

where n_e is the electron number density. The characteristic Hall timescale is

$$t_{\text{Hall}} = \frac{4\pi n_e e L^2}{cB}, \quad (12)$$

where L and B are the typical length scale and field strength. Using values $n_e \sim 10^{35} \text{ cm}^{-3}$, $L \sim 0.5H$, with H the crust thickness ~ 1 km, and $B \sim 2 \times 10^{14}$ G, we find $t_{\text{Hall}} \sim 8$ kyr. We can further evaluate the Hall timescale as a function of location in the crust via $t_{\text{Hall}} \sim |\mathbf{B}|/|\partial \mathbf{B}/\partial t|$. We find that the Hall time scale is greater than 10 kyr throughout most of the crust, and decreases to a value of 5 kyr at the edges of the crust. Thus,

the magnetic field configuration is stable enough to remain virtually unchanged up to more than the current age of the NS (about 7 kyr).

5. CONCLUSION

This paper has two main results:

(i) We have developed a general-purpose method (“Temperature Template with Full Transport”, TTFT) to efficiently compute the radiation intensity from different patches of a NS surface with arbitrary magnetic fields and effective temperatures. The TTFT method accounts for the effects of realistic polarized photon opacities and anisotropic radiative transport in NS atmospheres without self-consistent atmosphere modeling for every surface patch. This method is therefore useful for computing synthetic light curves of X-ray emission from the whole neutron star surface.

(ii) We have used the TTFT method to model the X-ray light curve of the young NS in the Kes 79 supernova remnant. We find that a crustal magnetic field of order a few $\times 10^{14}$ G, much stronger than the observed dipole field, can produce significant surface temperature inhomogeneity and generate the observed large pulse fraction. Small hot spots can be produced even for fields that vary smoothly from the magnetic poles to the equator. Although our specific crustal field model adopts a conservative axisymmetric toroidal configuration, we believe that our general conclusion about the strength of the hidden magnetic field in the star’s crust is robust for more general field configurations.

Although we have developed the TTFT method with the application to the Kes 79 NS in mind, the basic methodology may prove useful for wider applications. In many published works on surface emission from magnetic NSs, the observed radiation is compared to a single-temperature NS atmosphere model, while in reality, a synthetic radia-

tion flux from the whole star is needed. Using the TTFT method, the total radiation from different patches of the NS may be calculated with temperature templates from a small number of self-consistent atmosphere models. We have shown in this paper that at least with respect to the light curves, the TTFT method can produce accurate result.

Our finding that the Kes 79 NS has a much larger hidden magnetic field in the crust than the dipole field inferred from the spindown measurement (see Halpern & Gotthelf 2010) may have important implications for the nature of central compact objects (CCOs) and the evolution of NS magnetic fields. CCOs constitute a significant population of NSs in supernova remnants. Recent observations have shown that the 7-10 known CCOs (or candidates) have weak dipole magnetic fields (Halpern & Gotthelf 2010,2011), so their relationship to other types of isolated NSs (radio pulsars, magnetars and dim isolated NSs) is unclear (van Kerkwijk & Kaplan 2007; Kaspi 2010). The presence of a large sub-surface magnetic field in the Kes 79 NS supports the notion that supernova fallback may have submerged the magnetic field, which may later diffuse back to the surface (e.g., Muslimov & Page 1995; Geppert et al. 1999; Ho 2011). Together, this property of the Kes 79 NS and the recent discovery of SGR 0418+5729 with a weak dipole field (Rea et al. 2010; Turolla et al. 2011) suggest that both the hidden sub-surface magnetic field and the “visible” dipole field of NSs play an important role in their observational manifestations.

We thank Wynn Ho and Valery Suleimanov for supplying their neutron star atmosphere models, which are essential for calibrating our method. We also thank Wynn Ho, Alexander Potekhin and Marten van Kerkwijk for useful discussion and suggestions. This work was supported in part by NSF grant AST-1008245 and NASA grant NNX10AP19G.

REFERENCES

- Beloborodov, A.M. 2002, ApJ, 566, 85
 Braithwaite, J. 2009, MNRAS, 397, 763
 Braithwaite, J., & Nordlund, A. 2006, A&A, 450, 1077
 Contopoulos, I., & Spitkovsky, A. 2006, ApJ, 643, 1139
 Geppert, U., Kueker, M., Page, D. 2004, A&A, 426, 267
 Geppert, U., Kueker, M., Page, D. 2006, A&A, 457, 937
 Geppert, U., Page, D., & Zannias, T. 1999, A&A, 345, 847
 Halpern, J.P., & Gotthelf, E.V. 2010, ApJ, 709, 436
 Halpern, J.P., & Gotthelf, E.V. 2011, ApJ, 733, L28
 Heyl, J.S., & Hernquist, L. 1998, MNRAS, 300, 599
 Ho, W.C.G. 2007, MNRAS, 380, 71
 Ho, W.C.G. 2011, MNRAS, 414, 2567
 Ho, W.C.G., & Lai, D. 2001, MNRAS, 327, 1081
 Ho, W.C.G., & Lai, D. 2003, MNRAS, 338, 233
 Ho, W.C.G., & Lai, D. 2004, ApJ, 607, 420
 Kaspi, V.M., 2010, Pub. Nat. Acad. Sci., 107, 7147
 Lai, D., & Ho, W.C.G. 2002, ApJ, 566, 373
 Lai, D., & Ho, W.C.G. 2003, ApJ, 588, 962
 Lai, D., & Salpeter, E.E. 1997, ApJ, 491, 270
 Medin, Z., & Lai, D. 2007, MNRAS, 382, 1833
 Muslimov, A., & Page, D. 1995, ApJ, 440, L77
 Pavlov, G.G., Shibano, Y.A., Zavlin, V.E., & Meyer, R.D. 1995, in Proc. NATO Advanced Study Institute on The Lives of Neutron Stars, ed. M.A. Alpar, U.Kiziloglu, & J. van Paradijs (Dordrecht: Kluwer), 71
 Pons, J.A., & Geppert, U. 2007, A&A, 470, 303
 Pons, J.A., Miralles, J.A., & Geppert, U. 2009, A&A, 496, 207
 Potekhin, A.Y. 2010, A&A, 518, A24
 Potekhin, A.Y., Lai, D., Chabrier, G., & Ho, W.C.G. 2004, ApJ, 612, 1034
 Potekhin, A.Y., & Yakovlev, D.G. 2001, A&A, 374, 213
 Potekhin, A.Y., Yakovlev, D.G., Chabrier, G., Gnedin, O.Y., 2003, ApJ, 594, 404
 Poutanen, J. & Beloborodov, A. M. 2006, MNRAS, 373, 836
 Rea, N., et al. 2010, Science, 330, 944
 Reisenegger, A. 2009, A&A, 499, 557
 Reisenegger, A., Prieto, J.P., Benguria, R., Lai, D., & Araya, P.A. 2005, in AIP Conf. Proc. 784, The Magnetic Fields in the Universe (Melville, NY: AIP), 263 (arXiv:astro-ph/0503047)
 Schaaf, M.E. 1990, A&A, 227, 61
 Shibano, I.A., Zavlin, V.E., Pavlov, G.G., & Ventura, J. 1992, A&A, 266, 313
 Suleimanov, V., Hambaryan, V., Potekhin, A.Y., et al. 2010, A&A, 522, A111
 Thompson, C., & Duncan, R.C. 2001, ApJ, 561, 980
 Turolla, R., 2009, in Neutron Stars and Pulsars (Astrophysics and Space Science Library, Vol. 357; Berlin: Springer), 141
 Turolla, R., Zane, S., Pons, J.A., Esposito, P., & Rea, N. 2011, ApJ, 740, 105
 van Adelsberg, M., & Lai, D. 2006, MNRAS, 373, 1495
 van Kerkwijk, M.H., & Kaplan, D.L. 2007, Ap&SS, 308, 191
 Zane, S., & Turolla, R. 2006, MNRAS, 366, 727
 Zane, S., Turolla, R., Stella, L., & Treves, A. 2001, ApJ, 560, 384